PHYSICAL REVIEW B **89**, 235311 (2014)

Atomistic modeling of coupled electron-phonon transport in nanowire transistors

Reto Rhyner* and Mathieu Luisier†
Integrated Systems Laboratory, ETH Zürich, Gloriastr. 35, 8092 Zürich, Switzerland

(Received 18 March 2014; revised manuscript received 6 May 2014; published 13 June 2014)

Self-heating effects are investigated in ultrascaled gate-all-around silicon nanowire field-effect transistors (NWFETs) using a full-band and atomistic quantum transport simulator where electron and phonon transport are fully coupled. The nonequilibrium Green's function formalism is used for that purpose, within a nearest-neighbor $sp^3d^5s^*$ tight-binding basis for electrons and a modified valence-force-field model for phonons. Electron-phonon and phonon-electron interactions are taken into account through specific scattering self-energies treated in the self-consistent Born approximation. The electron and phonon systems are driven out of equilibrium; energy is exchanged between them while the total energy current remains conserved. This gives rise to local variations of the lattice temperature and the formation of hot spots. The resulting self-heating effects strongly increase the electron-phonon scattering strength and lead to a significant reduction of the ON-current in the considered ultrascaled Si NWFET with a diameter of 3 nm and a length of 45 nm. At the same time, the lattice temperature exhibits a maximum close to the drain contact of the transistor.

DOI: 10.1103/PhysRevB.89.235311 PACS number(s): 73.63.−b, 72.10.−d, 63.22.−m, 63.20.kd

I. INTRODUCTION

The continued miniaturization of the transistor dimensions according to Moore's scaling law [1] has led to an impressive evolution of the electronic device functionalities. By reducing the size of the transistors a significant improvement of their electrical performance is obtained. On the negative side, since their supply voltage has stopped scaling as fast as their dimensions, heat dissipation has kept increasing from one generation to the other [2]. Consequently, the power density of integrated circuits (ICs) is dangerously approaching the 150 $\mathrm{W/cm^2}$ limit up to which air can be used to cool the device temperature [3]. The recent replacement of the two-dimensional planar Si metal-oxide-semiconductor field-effect transistors (MOSFETs) by three-dimensional FinFETs [4] has momentarily stabilized the increase in heat dissipation and IC power consumption. FinFETs indeed show a decrease of their passive power component as compared to two-dimensional (2D) MOSFETs due to the better electrostatic control provided by their triple gate configuration.

In the future FinFETs might evolve towards ultrascaled gate-all-around nanowire field-effect transistors (GAA NWFETs) [5–10]. Because of the superior electrostatic control of a surrounding gate the electrical performance of GAA NWFETs outperforms that of FinFETs. While the static and dynamic aspects of NWFETs have received a lot of attention, their electrothermal properties have not been thoroughly investigated so far, although they might be the limiting factor in such devices [11]! Nanowires exhibit a reduced thermal conductivity as compared to bulk structures [12–14], which represents a fertile ground for the formation of localized hot spots and self-heating effects.

The narrow dimensions of ultrascaled NWFETs make it difficult to measure an internal temperature distribution or a power dissipation profile [15]. Hence, it is challenging to experimentally investigate the influence of self-heating and hot spots on the characteristics of future nanotransistors. As a technology enabler physics-based device simulations can be used to support the experimental work and compute the electrothermal properties of a given structure. However, the selected simulation approach must go beyond the computationally efficient classical drift-diffusion (DD) [16] model or the semiclassical Boltzmann transport equation (BTE) [11,17]. It must correctly cover all the quantum mechanical phenomena present at the nanoscale, especially tunneling, energy quantization, and geometrical confinement. To account for these effects and treat thermal transport at the phonon level a full-band and atomistic device simulator capable of handling both electrons and phonons is needed. There have been some attempts to combine electron and phonon transport in an atomistic basis, but they have been restricted to molecular junctions with a small number of atoms [18,19].

A fully coupled electron and phonon transport approach based on the nonequilibrium Green's function formalism (NEGF) is therefore proposed here. It can deal with three-dimensional nanowire transistors composed of several thousand atoms [20]. The electron properties are expressed in a $sp^3d^5s^*$ tight-binding basis while the phonon ones are described in a modified valence-force-field model. The NEGF formalism provides a natural treatment of the electron-phonon and phonon-electron interactions through scattering self-energies solved in the self-consistent Born approximation. These scattering self-energies drive both the electron and phonon populations out of equilibrium and allow for the consideration of coupled electrothermal transport phenomena such as self-heating or localized hot spots. The resulting improvement in the simulation accuracy can be compared to that brought by the extension of the drift-diffusion approach with an energy-balance and electrothermal model [21].

As an application, self-heating effects are investigated in a Si GAA NWFET with a diameter of 3 nm, a total length of 45 nm, and composed of more than 15 000 atoms. These results are compared to the case where the electrons are coupled to equilibrium phonons at room temperature. It is shown that for reasonably high electron currents the power dissipated by phonon emission leads to a significant

---

*rhyner@iis.ee.ethz.ch
†mluisier@iis.ee.ethz.ch

increase of the phonon population through the entire device. Furthermore the nonequilibrium phonon distribution causes a strong enhancement of the electron-phonon coupling strength and therefore a noticeable reduction of the electron current. To better quantify the self-heating, an effective lattice temperature is introduced and calculated in the selected NW structure. Its spatial distribution demonstrates the formation of hot spots that are clearly related to the shape of the phonon population.

The paper is organized as follows: In Sec. II, the simulation approach is introduced, starting from the electron and phonon NEGF equations, their interactions, and the calculation of energy currents. Details about the numerical implementation are given in the Appendix. In Sec. III the fully coupled electron-phonon transport model is applied to a Si GAA NWFET where self-heating effects are investigated and an effective lattice temperature extracted. The paper is concluded in Sec. IV and an outlook on possible future works is proposed.

II. THEORY

Electron and phonon transport are treated in the framework of the NEGF formalism under steady-state conditions, i.e., all the Green's functions are solved in the energy (frequency) domain and not as a function of the time. The targeted structures are Si circular nanowires surrounded by an oxide layer that does not take part in the transport calculations. The electrons and phonons can only enter or escape the simulation domain at both ends of the nanowire and not at its surface. In particular, thermal losses through the oxide are not included.

A. Electron model

The NEGF equations for electrons are expressed in a nearest-neighbor tight-binding basis where the lesser ($G^<$), greater ($G^>$), and retarded (G^R) Green's functions have the following form in a nanowire structure [22]:

$$\sum_l ((\mathbf{E}-\mathbf{V}(\mathbf{R}_m))\delta_{lm} - \mathbf{H}_{ml} - \boldsymbol{\Sigma}^{\mathrm{RB}}_{ml}(E) - \boldsymbol{\Sigma}^{\mathrm{RS}}_{ml}(E))\mathbf{G}^R_{ln}(E) = \delta_{mn}, \tag{1}$$

$$\mathbf{G}^{\gtrless}_{nm}(E) = \sum_{l_1 l_2} \mathbf{G}^R_{nl_1}(E)\big(\boldsymbol{\Sigma}^{\gtrless B}_{l_1 l_2}(E) + \boldsymbol{\Sigma}^{\gtrless S}_{l_1 l_2}(E)\big)\mathbf{G}^{R\dagger}_{ml_2}(E), \tag{2}$$

$$\boldsymbol{\Sigma}^R_{nm}(E) = \frac{1}{2}(\boldsymbol{\Sigma}^>_{nm}(E) - \boldsymbol{\Sigma}^<_{nm}(E)) + i\mathcal{P}\int \frac{dE'}{2\pi}\frac{\boldsymbol{\Sigma}^>_{nm}(E') - \boldsymbol{\Sigma}^<_{nm}(E')}{E-E'}. \tag{3}$$

In Eq. (3), $\mathcal{P}$ denotes the Cauchy principal integral value. The indices n,m,l,l_1, and l_2 run over all atomic positions. The matrices $\mathbf{E}$ (diagonal, injection energy), $\mathbf{V}(\mathbf{R}_n)$ (diagonal, self-consistent electrostatic potential at position $\mathbf{R}_n$), $\mathbf{H}_{mn}$ (tight-binding matrix elements, on-site energy if $m = n$, nearest-neighbor coupling between atom m and n otherwise), $\boldsymbol{\Sigma}^B_{mn}(E)$ (electron boundary self-energy, different from 0 only if atoms m and n are directly connected to the semi-infinite leads, computed as in Ref. [23]), $\boldsymbol{\Sigma}^S_{mn}(E)$ (electron-phonon scattering self-energy between atoms m and n modeling the coupling to the phonon system), and $\mathbf{G}_{nl}(E)$ (electron Green's functions between atoms n and l) are of size $N_{\mathrm{orb}} \times N_{\mathrm{orb}}$, where N_{orb} is the number of orbitals of the tight-binding model. In this work a $sp^3d^5s^*$ basis without spin-orbit coupling is used to describe the Si properties [24], i.e., $N_{\mathrm{orb}} = 10$. The definition and the interpretation of the tight-binding Hamiltonian blocks $\mathbf{H}_{mn}$ can be found in Ref. [25]. In this approach, each atom is treated individually so that the size of the linear system of equations in Eqs. (1) and (2) is equal to $N_A \times N_{\mathrm{orb}}$, N_A being the total number of atoms in the Si channel. Hard wall boundary conditions are applied at the nanowire surface [26].

B. Phonon (thermal) model

For the phonons the NEGF equations look as follows [27]:

$$\sum_l \big(M_m\omega^2\delta_{lm} - \boldsymbol{\Phi}_{ml} - \boldsymbol{\Pi}^{\mathrm{RB}}_{ml}(\omega) - \boldsymbol{\Pi}^{\mathrm{RS}}_{ml}(\omega)\big)\mathbf{D}^R_{ln}(\omega) = \delta_{mn}, \tag{4}$$

$$\mathbf{D}^{\gtrless}_{nm}(\omega) = \sum_{l_1 l_2} \mathbf{D}^R_{nl_1}(\omega)\big(\boldsymbol{\Pi}^{\gtrless B}_{l_1 l_2}(\omega) + \boldsymbol{\Pi}^{\gtrless S}_{l_1 l_2}(\omega)\big)\mathbf{D}^{R\dagger}_{ml_2}(\omega), \tag{5}$$

$$\boldsymbol{\Pi}^R_{nm}(\omega) = \frac{1}{2}(\boldsymbol{\Pi}^>_{nm}(\omega) - \boldsymbol{\Pi}^<_{nm}(\omega)) + i\mathcal{P}\int \frac{d\omega'}{2\pi}\frac{\boldsymbol{\Pi}^>_{nm}(\omega') - \boldsymbol{\Pi}^<_{nm}(\omega')}{\omega-\omega'}. \tag{6}$$

Similar to the electron case the indices n,m,l,l_1, and l_2 run over all the atomic positions. The matrices ω^2 (diagonal, ω is the phonon frequency), $\boldsymbol{\Phi}_{mn}$ (dynamical matrix block corresponding to the second derivative of the harmonic potential with respect to m and n), $\boldsymbol{\Pi}^B_{mn}(\omega)$ (phonon boundary self-energy between atom m and n, only different from 0 when m and n are directly connected to the semi-infinite leads, computed with the same "shift-and-invert" scheme as the electron boundary self-energy [23], except that the structure of the involved matrices changes due to the presence of beyond nearest-neighbor connections), $\boldsymbol{\Pi}^S_{mn}(\omega)$ (phonon-electron scattering self-energy between atoms m and n describing the coupling to the electron system), and $\mathbf{D}_{nl}(\omega)$ (phonon Green's functions between atoms n and l) are of size 3×3 where 3 is the number of degrees of freedom per atom, i.e., the number of directions along which atoms can oscillate (x, y, and z). The entries of the dynamical matrix $\boldsymbol{\Phi}_{mn}$ are approximated as

$$\Phi^{ij}_{mn} = \frac{d^2V^{\mathrm{harm}}}{dR^i_m dR^j_n}, \tag{7}$$

the second derivative of the valence-force-field (VFF) harmonic potential energy V^{harm} with respect to the i^{th} and j^{th} components (x, y, and z) of the atom positions R_m and R_n. For an accurate reproduction of the phonon band structure of group IV semiconductors, the VFF potential energy V^{harm} must include at least four bond interactions. More information about the construction of the dynamical matrix and the harmonic force constants of Si can be found in Refs. [28,29]. Here again, the N_A atoms composing the simulated structures have an individual treatment. The size of the system to be solved in Eqs. (4) and (5) is therefore $3 \times N_A$. The Si atoms at the nanowire surface can freely oscillate.

C. Electrothermal coupling

To derive the coupling between the electron and phonon population it is convenient to start from the total Hamiltonian operator in the second quantization,

$$\begin{aligned}\hat{H}(t) = &\sum_{nm}\sum_{\sigma_1\sigma_2} H_{mn}^{\sigma_1\sigma_2}\hat{c}_{m\sigma_1}^{\dagger}(t)\hat{c}_{n\sigma_2}(t)\\ &+\frac{1}{2}\sum_{n}\sum_{i} M_n\hat{\dot{u}}_n^i(t)\hat{\dot{u}}_n^i(t)\\ &+\frac{1}{2}\sum_{nm}\sum_{ij}\Phi_{mn}^{ij}\hat{u}_m^i(t)\hat{u}_n^j(t)\\ &+\sum_{nm}\sum_{\sigma_1\sigma_2}\sum_{i}\nabla_i H_{mn}^{\sigma_1\sigma_2}\hat{c}_{m\sigma_1}^{\dagger}(t)\hat{c}_{n\sigma_2}(t)\big(\hat{u}_n^i(t)-\hat{u}_m^i(t)\big).\end{aligned} \tag{8}$$

In Eq. (8) the indices i, j, and σ refer to the real space directions (x, y, and z) and the atomic orbitals (s, p, d, and s^*), respectively. The operator $\hat{c}_{m\sigma_1}^{\dagger}(t)$ ($\hat{c}_{m\sigma_1}(t)$) creates (annihilates) an electron with orbital σ_1 at position $\mathbf{R}_m$ and at time t, while $\hat{u}_m^i(t)$ is the phonon quantized displacement operator along the direction i at time t and at $\mathbf{R}_m$ with respect to the equilibrium atom position. The first term on the right-hand side of Eq. (8) is directly included in the tight-binding block $\mathbf{H}_{nm}$ in Eq. (1). The second (phonon-kinetic) and third (phonon-harmonic) terms appear in the dynamical matrix block $\mathbf{\Phi}_{nm}$ in Eq. (4). The last term in Eq. (8) connects the electron and phonon populations and is treated as a perturbation that is cast into the electron-phonon ($\mathbf{\Sigma}$) and phonon-electron ($\mathbf{\Pi}$) scattering self-energies. The presence of lattice vibrations where atoms oscillate around their equilibrium position $\mathbf{R}_m^0 \rightarrow \mathbf{R}_m(t) = \mathbf{R}_m^0 + \mathbf{u}_m(t)$ with the displacement vector $\mathbf{u}_m(t)$ induces the electron-phonon interactions [30,31]. To account for the atom oscillations the tight-binding Hamiltonian matrix $\mathbf{H}_{nm}$ is expanded in a Taylor series around the equilibrium bond vector $(\mathbf{R}_n^0 - \mathbf{R}_m^0)$ to the lowest order in the oscillations $\mathbf{u}_n(t) - \mathbf{u}_m(t)$:

$$\begin{aligned}\mathbf{H}_{mn} &\approx \mathbf{H}_{mn}^0 + \sum_i \frac{\delta\mathbf{H}_{mn}}{\delta(R_{n,i}^0 - R_{m,i}^0)}\big(u_n^i(t) - u_m^i(t)\big)\\ &\approx \mathbf{H}_{mn}^0 + \sum_i \nabla_i\mathbf{H}_{mn}\big(u_n^i(t) - u_m^i(t)\big).\end{aligned} \tag{9}$$

The transformation of the second term on the right-hand-side in Eq. (9) into the second quantization leads to the last operator in Eq. (8), representing the electron-phonon coupling. It still remains to determine an expression for the electron-phonon and phonon-electron scattering self-energies in Eqs. (1), (2), (4), and (5), respectively. To do that an equation of motion is derived for the time-dependent electron Green's function $G_{nm}^{\sigma_1\sigma_2}(t,t')$, which is proportional to the expectation value $\langle\hat{c}_{n\sigma_1}(t)\hat{c}_{m\sigma_2}^{\dagger}(t')\rangle$, and for the time-dependent phonon Green's function $D_{nm}^{ij}(t,t')$, which is proportional to $\langle\hat{u}_n^i(t)\hat{u}_m^j(t')\rangle$. The Hamiltonian operator $\hat{H}(t)$ in Eq. (8) is used for that purpose. As a next step the Wick's decomposition technique [32] is applied to truncate the arising infinite hierarchy of the equations of motion, the expectation value of two operators depending on three operators whose expectation value depends on four operators, and so forth. Langreth's theorem [33] is recalled to replace the general Green's functions with arguments on a complex time contour by real-time retarded, lesser, and greater Green's functions. Finally, after Fourier transforming the time difference $t - t'$, the steady-state form of the electron-phonon and phonon-electron scattering self-energy is obtained. For a detailed description of the derivation, see Appendix A. The greater or lesser components are defined as

$$\begin{aligned}\Sigma_{nm}^{\gtrless\sigma_1\sigma_2}(E) = i&\sum_{l_1l_2}\sum_{ij}\sum_{\sigma_3\sigma_4}\int_{-\infty}^{\infty}\frac{d(\hbar\omega)}{2\pi}\nabla_i H_{nl_1}^{\sigma_1\sigma_3}\\ &\times G_{l_1l_2}^{\gtrless\sigma_3\sigma_4}(E-\hbar\omega)\nabla_j H_{l_2m}^{\sigma_4\sigma_2}\big(D_{l_1m}^{\gtrless ij}(\omega)\\ &- D_{l_1l_2}^{\gtrless ij}(\omega) - D_{nm}^{\gtrless ij}(\omega) + D_{nl_2}^{\gtrless ij}(\omega)\big),\end{aligned} \tag{10}$$

$$\begin{aligned}\Pi_{nm}^{\gtrless ij}(\omega) = 2_{\text{spin}}\cdot i&\sum_{l_3l_4}\sum_{\sigma_1\sigma_2\sigma_3\sigma_4}\int_{-\infty}^{\infty}\frac{dE}{2\pi}\big(\nabla_i H_{l_3n}^{\sigma_3\sigma_1}\\ &\times G_{nl_4}^{\gtrless\sigma_1\sigma_4}(\hbar\omega+E)\nabla_j H_{l_4m}^{\sigma_4\sigma_2}G_{ml_3}^{\lessgtr\sigma_2\sigma_3}(E)\\ &- \nabla_i H_{l_3n}^{\sigma_3\sigma_1}G_{nm}^{\gtrless\sigma_1\sigma_2}(\hbar\omega+E)\nabla_j H_{ml_4}^{\sigma_2\sigma_4}G_{l_4l_3}^{\lessgtr\sigma_4\sigma_3}(E)\\ &- \nabla_i H_{nl_3}^{\sigma_1\sigma_3}G_{l_3l_4}^{\gtrless\sigma_3\sigma_4}(\hbar\omega+E)\nabla_j H_{l_4m}^{\sigma_4\sigma_2}G_{mn}^{\lessgtr\sigma_2\sigma_1}(E)\\ &+ \nabla_i H_{nl_3}^{\sigma_1\sigma_3}G_{l_3m}^{\gtrless\sigma_3\sigma_2}(\hbar\omega+E)\nabla_j H_{ml_4}^{\sigma_2\sigma_4}G_{l_4n}^{\lessgtr\sigma_4\sigma_1}(E)\big).\end{aligned} \tag{11}$$

Because spin-orbit coupling is not considered in the present calculations spin degeneracy is modeled via a factor two labeled 2_{spin}. The lesser self-energies $\mathbf{\Sigma}^<$ and $\mathbf{\Pi}^<$ are related to in-scattering processes, the greater ones $\mathbf{\Sigma}^>$ and $\mathbf{\Pi}^>$ to out-scattering [34]. More precisely, the lesser electron-phonon self-energy $\Sigma^<(E)$ describes for positive phonon energies ($\hbar\omega > 0$) the in-scattering of an electron from an occupied state $\mathbf{G}^<(E-\hbar\omega)$ at energy $E-\hbar\omega$ into an empty state at E. This happens through the absorption of an available phonon with energy $\hbar\omega$ whose occupancy is given by $\mathbf{D}^<(\omega)$. In the case $\hbar\omega < 0$ since $D_{nm}^{<ij}(-\omega) = D_{mn}^{>ji}(\omega)$ it follows that an electron in the occupied state $\mathbf{G}^<(E+|\hbar\omega|)$ at $E+|\hbar\omega|$ is transferred to E by a phonon emission. The probability of such transition depends on the availability of an empty phonon state at frequency ω, which is given by $\mathbf{D}^>(\omega)$. For the greater electron-phonon self-energy $\mathbf{\Sigma}^>(E)$ the situation is reversed, a positive (negative) phonon frequency ω corresponding to the out-scattering of an electron with energy E into a state with energy $E-\hbar\omega$ $(E+|\hbar\omega|)$ through phonon emission (absorption).

The phonon in- and out-scattering processes described by $\mathbf{\Pi}^<(\omega)$ and $\mathbf{\Pi}^>(\omega)$ behave slightly differently. An electron transition from an occupied state at energy E, $\mathbf{G}^<(E)$, to an empty state at $E+\hbar\omega$, $\mathbf{G}^>(E+\hbar\omega)$, requires the absorption of a phonon with energy $\hbar\omega$ and contributes to a decrease of the phonon population at this frequency (out-scattering). In-scattering involves an electron transition from $E+\hbar\omega$ to E through phonon emission, locally increasing the phonon count.

The scattering self-energies $\mathbf{\Sigma}(E)$ and $\mathbf{\Pi}(\omega)$ couple the electron and phonon baths because $\mathbf{\Sigma}(E)$ depends on $\mathbf{D}(\omega)$ and $\mathbf{\Pi}(\omega)$ on $\mathbf{G}(E)$. It clearly appears that the absorption or emission of a phonon does not only affect the electron population, but also the phonon one, which is not the case if the $\mathbf{\Pi}$ self-energies are ignored, as in most electron-phonon scattering treatments, e.g., Refs. [35–38]. It is also important to realize that the energy that is lost by the electrons does not vanish, but is captured by the phonons so that energy conservation is ensured. A careful verification of this property is critical for the accuracy of the results.

Equations (1)–(6), (10), and (11) must be solved iteratively until convergence between the Green's functions and the scattering self-energies is reached. This process is called self-consistent Born approximation. There is a second self-consistent loop between the Schrödinger and Poisson equations. Once convergence is achieved, the charge and current densities as well as the distribution of the phonon population are calculated as in Refs. [22,27]. Furthermore, the electron and phonon energy currents flowing between the s^{th} and $s^{\text{th}}+1$ slab (unit cell) of the simulated structures can be computed as

$$I_{el,s\to s+1} = \frac{2_{\text{spin}}}{\hbar}\sum_{n\in s}\sum_{m\in s+1}\sum_{\sigma_1\sigma_2}\int_{-\infty}^{\infty}\frac{dE}{2\pi}E\big(H_{nm}^{\sigma_1\sigma_2}G_{mn}^{<\sigma_2\sigma_1}(E) - G_{nm}^{<\sigma_1\sigma_2}(E)H_{mn}^{\sigma_2\sigma_1}\big), \tag{12}$$

and

$$I_{ph,s\to s+1} = \hbar\sum_{n\in s}\sum_{m\in s+1}\sum_{ij}\int_{0}^{\infty}\frac{d\omega}{2\pi}\omega\left(\Phi_{nm}^{ij}D_{mn}^{<ji}(\omega) - D_{nm}^{<ij}(\omega)\Phi_{mn}^{ji}\right). \tag{13}$$

In Eqs. (12) and (13), the atom position $\mathbf{R}_n$ is located in the s^{th} slab and $\mathbf{R}_m$ in the $s^{\text{th}}+1$ one. A slab contains an ensemble of N consecutive atomic layers along the direction of the current flow. For example, $N=4$ for transport along the $\langle 100\rangle$ crystal axis or $N=6$ for $\langle 111\rangle$. The total energy current must be conserved and constant through the entire device so that $I_{el,s\to s+1}+I_{ph,s\to s+1}$ remains the same for all possible s.

D. Simplifications and implementation

As already mentioned in Refs. [22,27] the electron-phonon ($\mathbf{\Sigma}$) and the phonon-electron ($\mathbf{\Pi}$) self-energies in Eqs. (10) and (11) are exact, but difficult to implement from a numerical point of view. To investigate fully coupled electron-phonon transport in realistic nanowire structures some simplifications must be applied to the calculation of $\mathbf{\Sigma}$ and $\mathbf{\Pi}$.

According to the arguments in Ref. [22] the electron-phonon scattering self-energies $\mathbf{\Sigma}_{nm}(E)$ are limited to on-site interactions only, i.e., $n=m$, but they remain blocks of size $N_{\text{orb}}\times N_{\text{orb}}$,

$$\Sigma_{nn}^{\gtrless\sigma_1\sigma_2}(E) = i\sum_{l\in NN(n)}\sum_{ij}\sum_{\sigma_3\sigma_4}\int_{-\infty}^{\infty}\frac{d(\hbar\omega)}{2\pi}\nabla_i H_{nl}^{\sigma_1\sigma_3}\times G_{ll}^{\gtrless\sigma_3\sigma_4}(E-\hbar\omega)\nabla_j H_{ln}^{\sigma_4\sigma_2}\big(D_{ln}^{\gtrless ij}(\omega) - D_{ll}^{\gtrless ij}(\omega) - D_{nn}^{\gtrless ij}(\omega) + D_{nl}^{\gtrless ij}(\omega)\big). \tag{14}$$

Reducing Eq. (14) to its simplest expression means omitting the nondiagonal phonon Green's function $\mathbf{D}_{nl}(\omega)$ and $\mathbf{D}_{ln}(\omega)$. However, ignoring $\mathbf{D}_{nl}(\omega)$ and $\mathbf{D}_{ln}(\omega)$ leads to an underestimation of the electron-phonon coupling strength that should be avoided.

Standard recursive Green's function (RGF) algorithms [39] are fully capable of producing $\mathbf{D}_{nl}(\omega)$ and $\mathbf{D}_{ln}(\omega)$ where $\mathbf{R}_l$ and $\mathbf{R}_n$ are nearest-neighbor positions, but the inclusion of these terms complicates the situation. The additional difficulty comes from the fact that to ensure energy conservation, beside the diagonal phonon-electron self-energies,

$$\Pi_{nn}^{\gtrless ij}(\omega) = -i\sum_{l}\sum_{\sigma_1\sigma_2\sigma_3\sigma_4}\int_{-\infty}^{\infty}\frac{dE}{2\pi}\big(\nabla_i H_{ln}^{\sigma_3\sigma_1}\times G_{nn}^{\gtrless\sigma_1\sigma_2}(\hbar\omega+E)\nabla_j H_{nl}^{\sigma_2\sigma_4}G_{ll}^{\lessgtr\sigma_4\sigma_3}(E) + \nabla_i H_{nl}^{\sigma_1\sigma_3}G_{ll}^{\gtrless\sigma_3\sigma_4}(\hbar\omega+E)\nabla_j H_{ln}^{\sigma_4\sigma_2}G_{nn}^{\lessgtr\sigma_2\sigma_1}(E)\big), \tag{15}$$

also the nondiagonal phonon-electron self-energies $\mathbf{\Pi}_{nl}(\omega)$ must be taken into account,

$$\Pi_{nl}^{\gtrless ij}(\omega) = i\sum_{\sigma_1\sigma_2\sigma_3\sigma_4}\int_{-\infty}^{\infty}\frac{dE}{2\pi}\big(\nabla_i H_{ln}^{\sigma_3\sigma_1}\times G_{nn}^{\gtrless\sigma_1\sigma_2}(\hbar\omega+E)\nabla_j H_{nl}^{\sigma_2\sigma_4}G_{ll}^{\lessgtr\sigma_4\sigma_3}(E) + \nabla_i H_{nl}^{\sigma_1\sigma_3}G_{ll}^{\gtrless\sigma_3\sigma_4}(\hbar\omega+E)\nabla_j H_{ln}^{\sigma_4\sigma_2}G_{nn}^{\lessgtr\sigma_2\sigma_1}(E)\big). \tag{16}$$

In Eq. (16), it is sufficient to consider the case where l is a nearest neighbor of n. To calculate $\mathbf{D}_{nl}(\omega)$ as needed in Eq. (14), the RGF algorithm used to solve Eqs. (4) and (5) must be extended to produce not only diagonal, but also nondiagonal entries, as described in Ref. [40]. A closer look at the parallel implementation of the NEGF equations is given in Appendix B. Note finally that in Eqs. (3) and (6), the principal integral term has been neglected in all the calculations reported in this paper. It contributes only to an energy renormalization, but not to relaxation or phase breaking and previous studies have also shown that this simplification does not significantly affect the device current [41,42].

III. RESULTS

A. Structure definition

As a simulation example, the Si GAA NWFET schematized in Fig. 1 is considered. The diameter of the NW measures 3 nm and it is surrounded by an oxide layer with a thickness $t_{ox}=3$ nm of HfO$_2$ characterized by a relative dielectric constant $\epsilon_r=20$ for an equivalent oxide thickness EOT $=$ 0.58 nm. The gate length L_g is set to 15 nm while the n-doped (donor concentration, $N_D=1\times10^{20}$ cm^{-3}) source and drain extensions measure 15 nm. The drain current flows along the x direction of the NWFETs, which is aligned with the $\langle 100\rangle$ crystal axis; y and z are directions of confinement. All the simulations are performed at room temperature (T_0) with a supply voltage $V_{DD}=0.6$ V. Room temperature means that the electrons (phonons) flowing into the NWFETs from the contacts obey an equilibrium Fermi-Dirac (Bose-Einstein) distribution function characterized by a temperature $T_0=$ 300 K. In contrast the outflowing electrons and phonons are rearranged due to scattering and the electrostatic potential

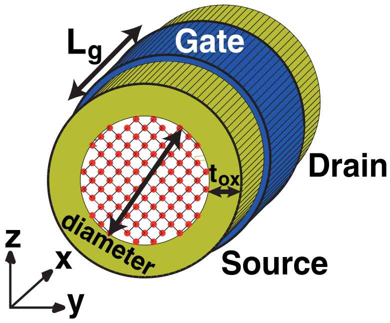

FIG. 1. (Color online) Schematic view of the n-type Si GAA NWFET simulated in this work. The gate length L_g measures 15 nm while the source and drain extensions have a length of 15 nm and a donor doping concentration fixed to $N_D = 1 \times 10^{20}$ cm^{-3}. The Si channel has a diameter of 3 nm and is surrounded by HfO$_2$ dielectric layers ($\epsilon_R = 20$) of thickness $t_{ox} = 3$ nm. The transport direction x is aligned with the $\langle 100\rangle$ crystal axis; y and z are directions of confinement. The total number of Si atoms in this structure is 16 019.

and therefore have a different distribution function and temperature.

The lowest conduction sub-bands (CB) and the first phonon branches of the free standing silicon nanowire are presented in Figs. 2(a) and 2(b), respectively. Due to geometrical confinement along the y and z directions the sixfold degenerate CB minimum of bulk Si is splitted into a group of four sub-bands at Γ (Δ_4) and two single bands at $k_x = \pm 2.08$ nm^{-1} (Δ_2). The transport effective mass is equal to $m^* = 0.29\, m_0$ for the Δ_4 group and $m^* = 0.92\, m_0$ for the Δ_2 bands. Quantum confinement does not only increase the band gap value from 1.12 to 1.62 eV, but also the transport effective mass from 0.2 to 0.29 m_0. For the phonons in Fig. 2(b) the group velocity of the purely longitudinal (LA) and transverse (TA) acoustic modes is reduced to 4600 m/s and 6300 m/s as compared to the bulk values of 5421 m/s and 8905 m/s, respectively. The influence of these modified electrothermal properties is investigated in the next subsections. In particular, the lower group velocities of the acoustic phonon branches make it difficult to evacuate the dissipated heat from nanowires and cause a strong increase in the lattice temperature.

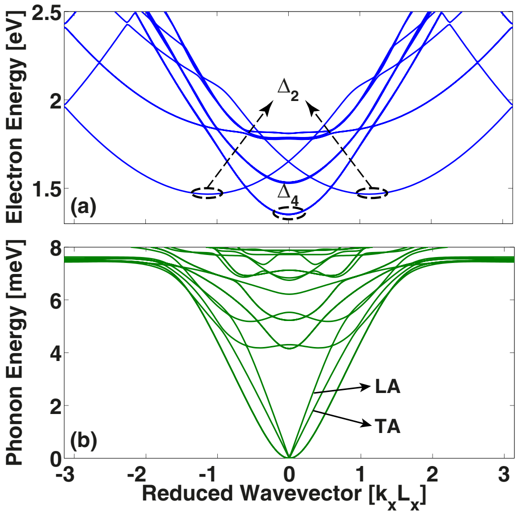

FIG. 2. (Color online) (a) Electron band structure for the same Si nanowire as in Fig. 1. The local minima are indicated with Δ_4 and Δ_2 where the subscripts define the degeneracy of the corresponding energy point. (b) Phonon band structure for the same Si nanowire as in (a). The purely longitudinal (LA) and transverse acoustic (TA) branches are indicated in the plot.

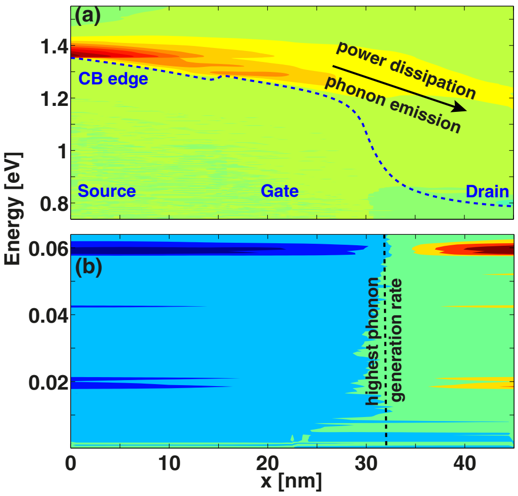

FIG. 3. (Color online) (a) Energy- and position-resolved electron current in the Si GAA NWFET of Fig. 1 at $V_{gs} = 0.6$ V and $V_{ds} = 0.6$ V. Red indicates high current concentrations and green no current. The dashed blue line refers to the position of the conduction band edge. (b) Energy- and position-resolved phonon energy current at the same bias conditions as in (a). Red indicates positive currents and blue negative ones. The black dashed line refers to the location with the highest phonon generation rate.

B. Electrothermal Effects

To illustrate the electrothermal effects occurring in an ultrascaled Si nanowire transistor, a specific bias point has been selected with a gate-to-source voltage $V_{gs} = 0.6$ V and a drain-to-source voltage $V_{ds} = 0.6$ V. The standard scattering approach where the electrons interact with equilibrium phonons characterized by a Bose-Einstein distribution and a constant temperature $T_0 = 300$ K, as in Ref. [22] is compared to the fully coupled electron and phonon transport model introduced in Sec. II. The electrical currents are labeled $I_{d,\mathrm{scatt}}$ in the standard case and $I_{d,\mathrm{self}}$ in the fully coupled one. At $V_{gs} = 0.6$ V and $V_{ds} = 0.6$ V, $I_{d,\mathrm{scatt}} = 9.32\ \mu$A and $I_{d,\mathrm{self}} = 6.06\ \mu$A. As explained later, the current reduction comes from self-heating effects.

The energy- and position-resolved electron and phonon currents are reported in Fig. 3 for the considered bias point with self-heating. In subplot Fig. 3(a), red indicates high current concentrations, green no current. It can be observed that electrons lose energy while flowing from the source (left) to the drain (right) contact. This happens through phonon emission. As a consequence, phonons are created, as shown in subplot (b) where red indicates a positive phonon energy current and blue a negative one. The current magnitude is higher around the bulk optical phonon frequency and around the frequency that corresponds to the transverse acoustic plateau in bulk Si.

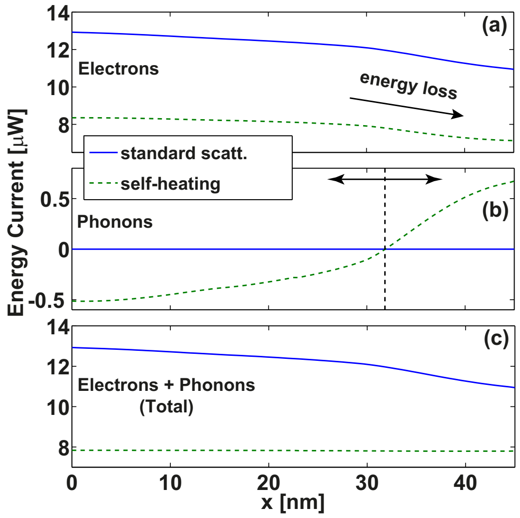

FIG. 4. (Color online) (a) Electron component of the energy current flowing through the same Si GAA NWFET as in Fig. 3. The standard scattering (equilibrium phonons, solid blue line) and the self-heating (nonequilibrium phonons, green dashed line) cases are shown. (b) Same as in (a) but for the phonon component of the energy current. (c) Same as in (a), but for the total energy current (electron+phonon).

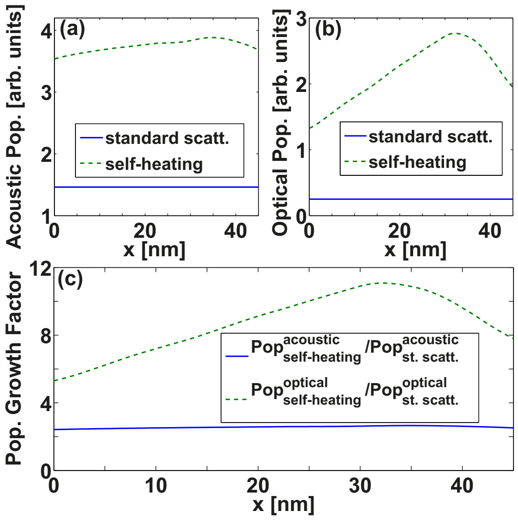

FIG. 5. (Color online) (a) Low frequency (or acoustic) and (b) high frequency (or optical) phonon population in the same Si GAA NWFET as before. The blue solid lines refer to the standard scattering case, the green dashed lines to the self-heating case. (c) Growth factor for the optical (green dashed line) and acoustic (blue solid line) phonon populations between self-heating and the standard scattering theory.

In nanowires, the emitted phonon has the same probability to propagate towards the source or drain extension. Hence, the current flow vanishes at the location with the highest phonon generation rate. There, the formation of a hot spot is expected.

By looking at the electron and phonon energy currents, as in Fig. 4, it is confirmed that (i) electrons lose energy between source and drain and (ii) close to the end of the nanowire, there is a position with no phonon current. The fundamental difference between the standard scattering theory of Ref. [22] and the coupled electron-phonon model presented here becomes also visible in Fig. 4. The power dissipated by electrons can only be captured by the phonons if the latter are driven out of equilibrium. In this case, the total (electron+phonon) energy current is conserved all along the transport axis of the nanowire, as demonstrated in Fig. 4(c). With equilibrium phonons, the energy lost by the electrons simply vanishes and energy conservation is broken. The total energy current is larger on the source than on the drain side. It is worthwhile noting that the phonon energy current is positive close to the end of the device, but negative in the rest of the simulation domain.

Another important difference between equilibrium ($ph_{\rm eq}$) and nonequilibrium ($ph_{\rm neq}$) phonons is shown in Fig. 5 where the spatially resolved low frequency ($\hbar\omega < 30$ meV, labeled "acoustic") and high frequency ($\hbar\omega > 30$ meV, "optical") phonon populations are reported as well as the ratio between $ph_{\rm neq}$ and $ph_{\rm eq}$. It can be seen that the acoustic phonon generation remains almost constant throughout the entire nanowire structure while the emission of optical phonons is larger close to the drain side. At the location of the highest generation rate, the optical phonon population increases by a factor of 10 as compared to the standard electron-phonon scattering theory. Close to the source, there is a growth by a factor 5 of the number of optical phonons. Since electrons interact more strongly with such phonons, as explained in Ref. [22], a higher optical phonon population causes more scattering events and therefore a reduction of the drain current from $I_{d,\rm scatt} = 9.32\ \mu$A down to 6.06 μA.

The energy- and position-resolved effective electron generation rate $G_{\rm el-eff}(E,\mathbf{R}_n)$, as depicted in Fig. 6, gives a different perspective on the involved physics. It is defined as $G_{\rm el-eff}(E,\mathbf{R}_n) = \frac{1}{\hbar}{\rm Tr}[\mathbf{G}^>_{nn}(E)\cdot\boldsymbol{\Sigma}^<_{nn}(E) - \boldsymbol{\Sigma}^>_{nn}(E)\cdot$

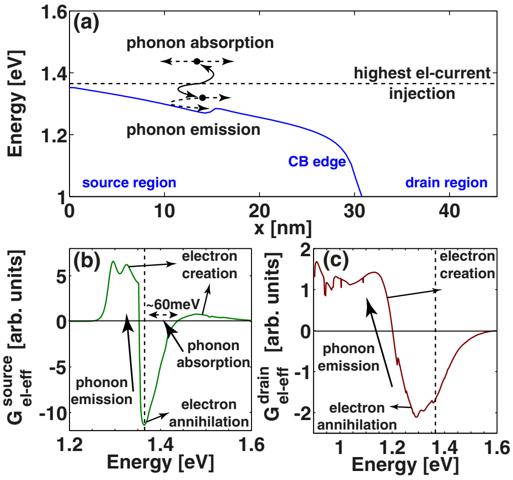

FIG. 6. (Color online) (a) Conduction band edge (solid blue line) of the Si GAA NWFET at $V_{gs} = 0.6$ V and $V_{ds} = 0.6$ V. The source and drain regions as well as the energy location with the highest spectral electron current [see Fig. 3(a), dashed black line] are indicated. (b) Energy-resolved effective electron scattering rate in the source region ($G^{\rm source}_{\rm el-eff}(E) \sim \sum_{n\in{\rm source}}\frac{1}{\hbar}{\rm Tr}[\mathbf{G}^>_{nn}(E)\cdot\boldsymbol{\Sigma}^<_{nn}(E) - \boldsymbol{\Sigma}^>_{nn}(E)\cdot\mathbf{G}^<_{nn}(E)]$). The dashed black line corresponds to the highest spectral electron current as in (a). (c) Same as in (b), but in the drain region.

$\mathbf{G}^{<}_{nn}(E)$]. A positive (negative) value indicates that in- (out-) scattering occurs at energy E and atom position $\mathbf{R}_n$. In other words, with $G_{\text{el-eff}}(E,\mathbf{R}_n) < 0$, electrons with energy E are annihilated at position $\mathbf{R}_n$, with $G_{\text{el-eff}}(E,\mathbf{R}_n) > 0$ electrons with energy E are created at $\mathbf{R}_n$. In subplot Fig. 6(b), $G_{\text{el-eff}}(E,\mathbf{R}_n)$ is shown in the source region ($0\ \text{nm} \leqslant x \leqslant 15\ \text{nm}$). At energies $1.354\ \text{eV} \leqslant E_{\text{out}} \leqslant 1.424\ \text{eV}$ corresponding to the maximum of the electron flow, as shown in Fig. 3, electrons are annihilated through phonon emission and optical phonon absorption. Hence, in-scattering happens for $1.27\ \text{eV} \leqslant E_{\text{in},1} \leqslant 1.353\ \text{eV}$ (phonon emission) and for $1.437\ \text{eV} \leqslant E_{\text{in},2} \leqslant 1.595\ \text{eV}$ (optical phonon absorption).

The momentum of the scattered electrons might change its direction so that the resulting back-scattering effect eventually reduces the current magnitude [43]. As indicated in Fig. 6(a) back-scattering has a higher probability to occur in combination with phonon absorption (50%). In the case of phonon emission the potential distribution prevents the back-scattered electrons from reaching the source contact and reducing the current magnitude. Unless they absorb a phonon, their only way out of the device is towards the drain side. As mentioned earlier, in the nonequilibrium case, the optical phonon population grows, thus increasing the in-scattering probability in the energy range $1.437\ \text{eV} \leqslant E_{\text{in},2} \leqslant 1.595$ eV. This causes the current reduction between $I_{d,\text{scatt}}$ and $I_{d,\text{self}}$. In Fig. 6(c), the out-scattering of high energy electrons through phonon emission in the drain region ($30\ \text{nm} \leqslant x \leqslant 45\ \text{nm}$) can be clearly identified. However, because the electrons have passed the critical length of the transistor [43], no further current reduction is induced by these scattering events.

C. Effective lattice temperature

To further quantify self-heating an effective lattice temperature (T_{eff}) is introduced. Because the considered NWFET structure is ultrascaled and in a nonequilibrium state the concept of temperature is questionable especially its direct relation to the thermodynamical quantity. Based on existing calculations of temperatures in molecular junctions [44,45] two approaches are proposed here to evaluate T_{eff}. They are compared to each other to validate the effective temperature concept. Both methods are intuitive measures of an atomistic temperature and coincide with the temperature in the thermodynamical limit.

(1) Population approach ($T^{\text{pop}}_{\text{eff}}$). In the first approach the temperature of a Bose-Einstein distribution function is adjusted to reproduce the same total phonon population [$N^{\text{tot}}_{\text{ph}}(\mathbf{R}_n)$] as obtained with the NEGF calculations,

$$\begin{aligned} N^{\text{tot}}_{\text{ph}}(\mathbf{R}_n) &= \int_0^\infty \frac{d(\hbar\omega)}{2\pi} N_{\text{Bose}}(\hbar\omega,T_{\text{eff}})\text{LDOS}(\omega,\mathbf{R}_n)\frac{2\hbar\omega}{\hbar^2} \\ &= \int_0^\infty \frac{d(\hbar\omega)}{2\pi} i\,\text{Tr}[\mathbf{D}^{<}_{nn}(\omega)]\frac{2\hbar\omega}{\hbar^2}, \end{aligned} \tag{17}$$

with the Bose-Einstein distribution function $N_{\text{Bose}}(\hbar\omega,T_{\text{eff}}) = \frac{1}{e^{\hbar\omega/k_B T_{\text{eff}}}-1}$ and the local density of states $\text{LDOS}(\omega,\mathbf{R}_n) = \text{Tr}[\mathbf{A}_{nn}(\omega)]$ where $\mathbf{A}_{nn}(\omega) = i[\mathbf{D}^{R}_{nn}(\omega) - \mathbf{D}^{A}_{nn}(\omega)] = i[\mathbf{D}^{>}_{nn}(\omega) - \mathbf{D}^{<}_{nn}(\omega)]$ is the spectral function. The variable $\mathbf{R}_n$ defines the lattice site at which the effective temperature T_{eff} is extracted.

(2) Probe approach ($T^{\text{probe}}_{\text{eff}}$). The second method is inspired by the fact that, experimentally, a temperature probe contacts the structure until thermal equilibrium is reached, i.e., until no net energy exchange occurs between the probe and the structure. The temperature probe is modeled by artificial phonon scattering self-energies $\mathbf{\Gamma}^{<>}_{nn}(\omega)$ chosen in such a way that no net energy current flows at the lattice site $\mathbf{R}_n$, i.e., in- and out-scattering compensate each other,

$$\begin{aligned} &\int_0^\infty \frac{d(\hbar\omega)}{2\pi}\hbar\omega\text{Tr}[\mathbf{\Gamma}^{>}_{nn}(\omega)\cdot\mathbf{D}^{<}_{nn}(\omega)] \\ &\quad = \int_0^\infty \frac{d(\hbar\omega)}{2\pi}\hbar\omega\text{Tr}[\mathbf{D}^{>}_{nn}(\omega)\cdot\mathbf{\Gamma}^{<}_{nn}(\omega)]. \end{aligned} \tag{18}$$

These calculations are done in a postprocessing step. First the phonon Green's functions are computed without the $\mathbf{\Gamma}$ self-energies, as highlighted in the previous section. They are then used to solve Eq. (18). For that purpose, the $\mathbf{\Gamma}^{<>}_{nn}$ are assumed to have the following form (similar to Ref. [44] and Büttiker probes [46]):

$$\mathbf{\Gamma}^{>}_{nn}(\omega) = -i\,(N_{\text{Bose}}(\hbar\omega,T_{\text{eff}})+1)\,\mathbf{A}_{nn}(\omega)v_{\text{coup}}, \tag{19}$$

$$\mathbf{\Gamma}^{<}_{nn}(\hbar\omega) = -i\,N_{\text{Bose}}(\hbar\omega,T_{\text{eff}})\mathbf{A}_{nn}(\omega)v_{\text{coup}}. \tag{20}$$

The strength of the v_{coup} coupling between the probe and the atomic system is not relevant since it cancels out in Eq. (18). Again, the temperature of the Bose-Einstein distribution in Eqs. (19) and (20) is adjusted to fulfill Eq. (18).

The value of the effective temperature $T^{\text{pop}}_{\text{eff}}$ and $T^{\text{probe}}_{\text{eff}}$ averaged over a nanowire slab is reported in Fig. 7. For the coupled electrothermal transport model the structure is divided into 83 slabs and each slab contains 193 atoms. Beside $V_{gs} = 0.6$ V the cases $V_{gs} = 0.4$ V and $V_{gs} = 0.0$ V are also presented. The good agreement between the two computational approaches supports the definition of the effective lattice temperature. Two important facts should be

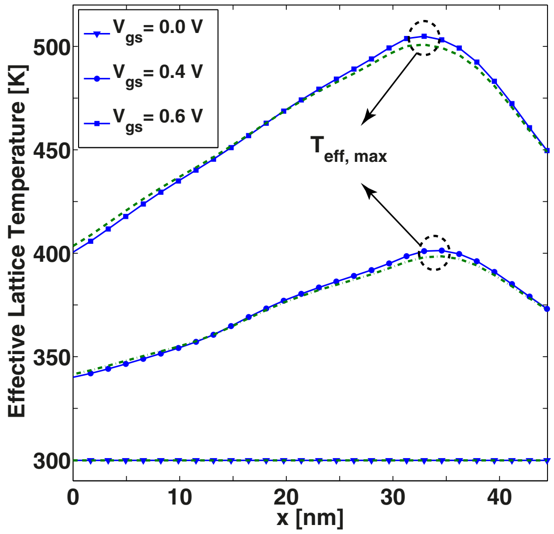

FIG. 7. (Color online) Effective lattice temperature averaged over a nanowire slab in the structure described in Fig. 1. It is calculated according to the population (solid blue lines with symbols, $T^{\text{pop}}_{\text{eff}}$) and the probe approach (green dashed lines, $T^{\text{probe}}_{\text{eff}}$). Three gate biases $V_{gs} = 0.0$ V, $V_{gs} = 0.4$ V, and $V_{gs} = 0.6$ V are considered.

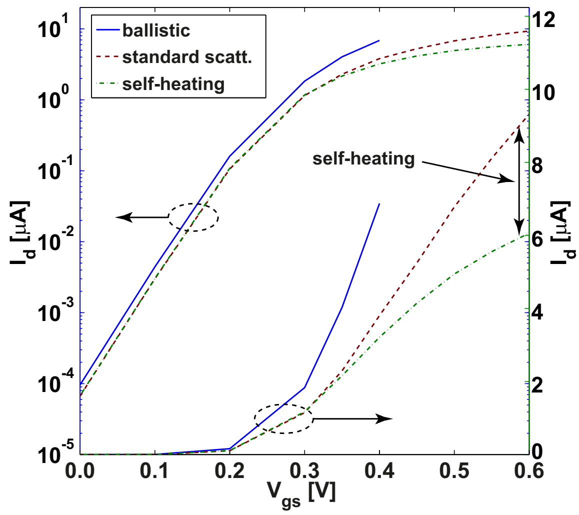

FIG. 8. (Color online) Transfer characteristics I_d-V_{gs} at $V_{ds} = 0.6$ V of the Si GAA NWFET in Fig. 1. The ballistic (blue solid line), standard scattering ($I_{d,\text{scatt}}$, red dashed line), and self-heating ($I_{d,\text{self}}$, green dashed-dotted line) currents are plotted. The influence of self-heating is indicated by the double arrow. Note that ballistic simulations do not converge at high gate voltages.

emphasized. At low V_{gs}, when the electrical current is too small to generate phonons at a high rate, the temperature remains constant and equal to 300 K in the entire nanowire structure. At $V_{gs} = 0.4$ V and $V_{gs} = 0.6$ V, the effective lattice temperature considerably increases and exhibits a peak close to the drain side, in accordance with the results from Figs. 3(a), 3(b), and 5. The peak location corresponds to the point where the phonon energy current changes its sign and where the optical and acoustic phonon populations reach a maximum. The values of T_{eff} at $V_{gs} = 0.4$ V and $V_{gs} = 0.6$ V indicate self-heating effects. In the standard electron-phonon scattering theory, T_{eff} would not increase with V_{gs}, but always stay equal to 300 K.

D. Device characteristics

Finally, the intrinsic transfer characteristics of the investigated Si GAA nanowire transistor are plotted in Fig. 8. Three different currents can be identified: (i) in the ballistic limit of transport ($I_{d,\text{bal}}$), (ii) computed with the standard scattering method ($I_{d,\text{scatt}}$), and (iii) with self-heating ($I_{d,\text{self}}$). Despite the short gate length of 15 nm Fig. 8 shows that the transistor does not operate close to its ballistic limit, neither with an equilibrium nor with a nonequilibrium phonon distribution. Turning on electron-phonon scattering reduces the current magnitude by about 45% at $V_{gs} = 0.4$ V as compared to the ballistic case. Driving the phonons out-of-equilibrium further decreases the current by another 30% at $V_{gs} = 0.6$ V, as indicated by the double arrow in Fig. 8. Hence, the total current reduction is roughly 50% in the presence of self-heating.

Two other physical quantities can be extracted from the coupled electrothermal transport simulations: the electrical power dissipated as heat and the maximum effective lattice temperature in the nanowire. The first one is defined as the difference between the electrical energy current at source and drain. The second corresponds to the lattice temperature at the location with the highest phonon generation rate. Both quantities are shown in Fig. 9 as a function of V_{gs}. The threshold voltage at which the dissipated power and the maximum temperature start to rapidly increase, $V_{gs} = 0.3$ V, is directly related to the point in Fig. 8 where self-heating starts to affect the current magnitude. After this turn-on, the dissipated power almost linearly increases up to $V_{gs} = 0.6$ V where it reaches a value larger than 1 μW. This, combined with an effective lattice temperature close to 500 K, suggests that thermal management will be a critical issue in future integrated circuits made of GAA NWFETs.

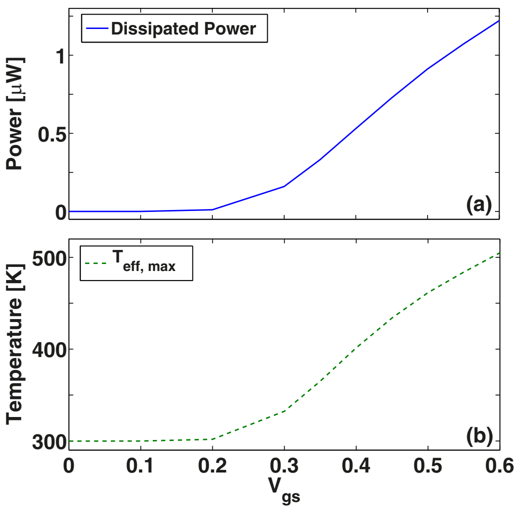

FIG. 9. (Color online) Evolution of the dissipated power (a) and the maximum effective temperature (b) as a function of V_{gs} for the Si GAA NWFET of Fig. 1.

IV. CONCLUSION AND OUTLOOK

Fully coupled electron-phonon transport has been treated in a full-band and atomistic device simulator based on the nonequilibrium Green's function formalism formulated in a nearest-neighbor tight-binding basis for electrons and in a modified valence-force-field basis for phonons. In this approach it has been possible to drive not only the electrons but also the phonons out-of-equilibrium to investigate self-heating effects in a Si gate all-around nanowire transistor with a diameter of 3 nm, a total length of 45 nm, and composed of more than 15 000 atoms. The simulation results have been compared to the case where electrons interact with equilibrium phonons characterized by a constant temperature of 300 K. It has been found that self-heating significantly increases the lattice temperature that can be mapped to the nonequilibrium phonon population. In addition, the higher phonon population has caused a strong enhancement of the electron-phonon coupling strength and a strong reduction of the electron current. It is therefore essential to take thermal management into account to design future electronic circuits relying on GAA NWFETs.

As future works, the influence of anharmonic phonon-phonon scattering on self-heating effects should be investigated. The optical phonon population might artificially accumulate in nanowires due to the missing decay of high frequency particles into low frequency ones. The redistribution of the phonon population towards more acoustic components is expected to decrease the electron-phonon coupling strength close to the source contact and lead to a slight increase of the current. Currently phonons can only escape at both ends of the nanowire and not at its surface, which could induce an overestimation of the lattice temperature values. The effect of the poor thermal conductivity of the surrounding oxide is partially compensated by the strongly reduced oxide thickness in these ultrascaled nanostructures. Hence, thermal losses at the gate contacts probably affect the temperature distribution and will be accounted for in a future study.

ACKNOWLEDGMENTS

This work was supported by SNF Grant No. PP00P2_133591, by a grant from the Swiss National Supercomputing Centre (CSCS) under Project No. s363, by NSF Grant No. EEC-0228390 that funds the Network for Computational Nanotechnology, by NSF PetaApps Grant No. 0749140, and by NSF through XSEDE resources provided by the National Institute for Computational Sciences (NICS).

APPENDIX A: SCATTERING SELF-ENERGIES

To calculate the scattering self-energies the starting point is the contour-ordered Green's function in the interaction picture because a systematic perturbation theory can be applied to it [33,39]:

$$G_{nm}^{\sigma_1\sigma_2}(\tau,\tau')\big[D_{nm}^{ij}(\tau,\tau')\big] = \frac{-i}{\hbar}\big\langle T_C e^{\frac{-i}{\hbar}\int_C d\tau'' \hat{H}_{\text{int}}(\tau'')}\hat{c}_{n\sigma_1}(\tau)\,\big[\hat{u}_n^i(\tau)\big]\,\hat{c}_{m\sigma_2}^{\dagger}(\tau')\,\big[\hat{u}_m^j(\tau')\big]\big\rangle, \tag{A1}$$

where **G** [**D**] is the electron [phonon] Green's function, T_C the contour ordering operator, C describes the Keldysh contour, and the brackets $\langle\cdots\rangle$ indicate the nonequilibrium ensemble average [47]. The $H_{\text{int}}(\tau)$ term is the not-exactly solvable perturbation Hamiltonian according to the last term in Eq. (8):

$$\hat{H}_{\text{int}}(\tau'') = \sum_{nm}\sum_{\sigma_1\sigma_2}\sum_{i}\nabla_i H_{mn}^{\sigma_1\sigma_2}\hat{c}_{m\sigma_1}^{\dagger}(\tau'')\hat{c}_{n\sigma_2}(\tau'')\big(\hat{u}_n^i(\tau'') - \hat{u}_m^i(\tau'')\big). \tag{A2}$$

The second quantized electron creation $\hat{c}_{n\sigma}^{\dagger}(\tau'')$ and annihilation $\hat{c}_{n\sigma}(\tau'')$ operators as well as the quantized lattice displacement $\hat{u}_n^i(\tau'')$ evolve according to the corresponding unperturbed Hamiltonian terms also described in Eq. (8). The noninteracting electron [phonon] Green's function can therefore be defined as

$$G_{nm}^{0,\sigma_1\sigma_2}(\tau,\tau')\big[D_{nm}^{0,ij}(\tau,\tau')\big] = \frac{-i}{\hbar}\big\langle T_C\hat{c}_{n\sigma_1}(\tau)\big[\hat{u}_n^i(\tau)\big]\hat{c}_{m\sigma_2}^{\dagger}(\tau')\big[\hat{u}_m^j(\tau')\big]\big\rangle. \tag{A3}$$

The scattering self-energies result from the expansion of the exponential in Eq. (A1) to the second order. The first-order term vanishes since the expectation value of an odd number of quantized lattice displacements is zero, $\langle u_n^i(\tau)\rangle = \langle u_{n_1}^{i_1}(\tau_1)u_{n_2}^{i_2}(\tau_2)u_{n_3}^{i_3}(\tau_3)\rangle = 0$. The irreducible scattering self-energy functional can be identified by writing the Dyson equation for the electron,

$$\mathbf{G}_{nm}(\tau,\tau') = \mathbf{G}_{nm}^0(\tau,\tau') + \int_C d\tau_1\int_C d\tau_2\sum_{n_1m_1}\mathbf{G}_{nn_1}^0(\tau,\tau_1)\boldsymbol{\Sigma}_{n_1m_1}(\tau_1,\tau_2)\mathbf{G}_{m_1m}(\tau_2,\tau'), \tag{A4}$$

and phonon Green's function,

$$\mathbf{D}_{nm}(\tau,\tau') = \mathbf{D}_{nm}^0(\tau,\tau') + \int_C d\tau_1\int_C d\tau_2\sum_{n_1m_1}\mathbf{D}_{nn_1}^0(\tau,\tau_1)\boldsymbol{\Pi}_{n_1m_1}(\tau_1,\tau_2)\mathbf{D}_{m_1m}(\tau_2,\tau'). \tag{A5}$$

In the self-consistent Born approximation the noninteracting Green's functions occurring in the expressions for the scattering self-energies are replaced by the full Green's functions as will be shown in the next section.

1. Electron-Phonon Scattering Self-Energy (Σ)

To evaluate the electron-phonon scattering self-energy **Σ** in Eq. (A4) the exponential in Eq. (A1) is expanded up to the second order,

$$G_{nm}^{\sigma_1\sigma_2}(\tau,\tau') = \frac{-i}{\hbar}\big\langle\hat{c}_{n\sigma_1}(\tau)\hat{c}_{m\sigma_2}^{\dagger}(\tau')\big\rangle + \frac{1}{2}\left(\frac{-i}{\hbar}\right)^3\int_C d\tau_1\int_C d\tau_2\langle\hat{H}_{\text{int}}(\tau_1)\hat{H}_{\text{int}}(\tau_2)\hat{c}_{n\sigma_1}(\tau)\hat{c}_{m\sigma_2}^{\dagger}(\tau')\rangle. \tag{A6}$$

Note that for brevity the contour-ordering operator T_C is omitted. By comparing Eqs. (A4) and (A6) it appears that the first term is equal to $G_{nm}^{0,\sigma_1\sigma_2}(\tau,\tau')$, while the second one contains information about the scattering self-energy. By replacing $\hat{H}_{\text{int}}(\tau'')$ with its value in Eq. (A2), the following expression is obtained:

$$\frac{1}{2}\left(\frac{-i}{\hbar}\right)^3 \int_C d\tau_1 \int_C d\tau_2 \sum_{n_1 m_1 n_2 m_2} \sum_{\sigma_3\sigma_4\sigma_5\sigma_6} \sum_{ij} \big\langle \nabla_i H_{m_1 n_1}^{\sigma_3\sigma_4} \nabla_j H_{m_2 n_2}^{\sigma_5\sigma_6} \hat{c}_{m_1\sigma_3}^{\dagger}(\tau_1) \hat{c}_{n_1\sigma_4}(\tau_1) \hat{c}_{m_2\sigma_5}^{\dagger}(\tau_2) \hat{c}_{n_2\sigma_6}(\tau_2) \hat{c}_{n\sigma_1}(\tau) \hat{c}_{m\sigma_2}^{\dagger}(\tau') \big\rangle$$

$$\times \big\langle \big(\hat{u}_{n_1}^i(\tau_1)\hat{u}_{n_2}^j(\tau_2) - \hat{u}_{n_1}^i(\tau_1)\hat{u}_{m_2}^j(\tau_2) - \hat{u}_{m_1}^i(\tau_1)\hat{u}_{n_2}^j(\tau_2) + \hat{u}_{m_1}^i(\tau_1)\hat{u}_{m_2}^j(\tau_2) \big) \big\rangle. \tag{A7}$$

Since the electron and phonon operators commute with each other, it is not important how they are arranged with respect to each other. To evaluate the expectation values $\langle \cdots \rangle$ Wick's decomposition technique [32] is used and only the relevant connected terms are kept

$$\frac{1}{2}\left(\frac{-i}{\hbar}\right)^3 \int_C d\tau_1 \int_C d\tau_2 \sum_{n_1 m_1 n_2 m_2} \sum_{\sigma_3\sigma_4\sigma_5\sigma_6} \sum_{ij} \Big(\nabla_i H_{m_1 n_1}^{\sigma_3\sigma_4} \nabla_j H_{m_2 n_2}^{\sigma_5\sigma_6} \big\langle \hat{c}_{n\sigma_1}(\tau) \hat{c}_{m_1\sigma_3}^{\dagger}(\tau_1) \big\rangle \big\langle \hat{c}_{n_1\sigma_4}(\tau_1) \hat{c}_{m_2\sigma_5}^{\dagger}(\tau_2) \big\rangle \big\langle \hat{c}_{n_2\sigma_6}(\tau_2) \hat{c}_{m\sigma_2}^{\dagger}(\tau') \big\rangle$$

$$+ \nabla_i H_{m_1 n_1}^{\sigma_3\sigma_4} \nabla_j H_{m_2 n_2}^{\sigma_5\sigma_6} \big\langle \hat{c}_{n\sigma_1}(\tau) \hat{c}_{m_2\sigma_5}^{\dagger}(\tau_2) \big\rangle \big\langle \hat{c}_{n_2\sigma_6}(\tau_2) \hat{c}_{m_1\sigma_3}^{\dagger}(\tau_1) \big\rangle \big\langle \hat{c}_{n_1\sigma_4}(\tau_1) \hat{c}_{m\sigma_2}^{\dagger}(\tau') \big\rangle \Big)$$

$$\times \big\langle \big(\hat{u}_{n_1}^i(\tau_1)\hat{u}_{n_2}^j(\tau_2) \big\rangle - \big\langle \hat{u}_{n_1}^i(\tau_1)\hat{u}_{m_2}^j(\tau_2) \big\rangle - \big\langle \hat{u}_{m_1}^i(\tau_1)\hat{u}_{n_2}^j(\tau_2) \big\rangle + \big\langle \hat{u}_{m_1}^i(\tau_1)\hat{u}_{m_2}^j(\tau_2) \big) \big\rangle. \tag{A8}$$

The contraction of the quantized lattice displacements is straight forward, whereas for the electron operators only two connected pairings remain. They can be merged together by interchanging the indices and introducing a factor two. Recalling the definition of the unperturbed Green's function in Eq. (A3) yields

$$i\hbar \int_C d\tau_1 \int_C d\tau_2 \sum_{n_1 m_1 n_2 m_2} \sum_{\sigma_3\sigma_4\sigma_5\sigma_6} \sum_{ij} G_{nm_1}^{0,\sigma_1\sigma_3}(\tau,\tau_1) \nabla_i H_{m_1 n_1}^{\sigma_3\sigma_4} G_{n_1 m_2}^{0,\sigma_4\sigma_5}(\tau_1,\tau_2) \nabla_j H_{m_2 n_2}^{\sigma_5\sigma_6} G_{n_2 m}^{0,\sigma_6\sigma_2}(\tau_2,\tau')$$

$$\times \left(D_{n_1 n_2}^{0,ij}(\tau_1,\tau_2) - D_{n_1 m_2}^{0,ij}(\tau_1,\tau_2) - D_{m_1 n_2}^{0,ij}(\tau_1,\tau_2) + D_{m_1 m_2}^{0,ij}(\tau_1,\tau_2) \right). \tag{A9}$$

By comparing Eqs. (A4) and (A9) the electron-phonon scattering self-energy can be identified as

$$\Sigma_{nm}^{\sigma_1\sigma_2}(\tau_1,\tau_2) = i\hbar \sum_{n_1 m_1} \sum_{\sigma_3\sigma_4} \sum_{ij} \nabla_i H_{nn_1}^{\sigma_1\sigma_3} G_{n_1 m_1}^{\sigma_3\sigma_4}(\tau_1,\tau_2) \nabla_j H_{m_1 m}^{\sigma_4\sigma_2}$$

$$\times \left(D_{n_1 m}^{ij}(\tau_1,\tau_2) - D_{n_1 m_1}^{ij}(\tau_1,\tau_2) - D_{nm}^{ij}(\tau_1,\tau_2) + D_{nm_1}^{ij}(\tau_1,\tau_2) \right). \tag{A10}$$

The noninteracting Green's functions can be replaced by the full Green's functions due to the implicit inclusion of higher order perturbation terms in Eq. (A4). To replace the complex-time contour arguments by real-time arguments Langreth's theorem [33] $C(\tau_1,\tau_2) = A(\tau_1,\tau_2)B(\tau_1,\tau_2) \rightarrow C^{\gtrless}(t_1,t_2) = A^{\gtrless}(t_1,t_2)B^{\gtrless}(t_1,t_2)$ is used. The consideration of steady-state situations allows for the Fourier transformation of the time difference $t_1 - t_2$. The electron-phonon scattering self-energy finally takes the following form:

$$\Sigma_{nm}^{\gtrless\sigma_1\sigma_2}(E) = i \sum_{n_1 m_1} \sum_{ij} \sum_{\sigma_3\sigma_4} \int \frac{d(\hbar\omega)}{2\pi} \nabla_i H_{nn_1}^{\sigma_1\sigma_3} G_{n_1 m_1}^{\gtrless\sigma_3\sigma_4}(E - \hbar\omega) \nabla_j H_{m_1 m}^{\sigma_4\sigma_2} \left(D_{n_1 m}^{\gtrless ij}(\omega) - D_{n_1 m_1}^{\gtrless ij}(\omega) - D_{nm}^{\gtrless ij}(\omega) + D_{nm_1}^{\gtrless ij}(\omega) \right). \tag{A11}$$

2. Phonon-Electron Scattering Self-Energy (Π)

For the calculation of the phonon-electron self-energy $\mathbf{\Pi}$ in Eq. (A5) the same approach as in the last section can be followed. However, a different solution based on the energy conservation condition is proposed here. The energy lost (gained) by the electrons $[+(-)Q_e]$ must be absorbed (emitted) by the phonons $[-(+)Q_{\text{ph}}]$ or in other words Q_e and Q_{ph} must compensate each other $Q_e + Q_{\text{ph}} = 0$ with

$$Q_e = \frac{1}{\hbar} \sum_{nm} \int \frac{dE}{2\pi} E \, \text{Tr}(\mathbf{\Sigma}_{nm}^{>}(E) \cdot \mathbf{G}_{mn}^{<}(E) - \mathbf{G}_{nm}^{>}(E) \cdot \mathbf{\Sigma}_{mn}^{<}(E)), \tag{A12}$$

and

$$Q_{\mathrm{ph}} = \frac{1}{\hbar}\sum_{nm}\int\frac{d(\hbar\omega)}{2\pi}\hbar\omega\mathrm{Tr}(\mathbf{\Pi}^{>}_{nm}(\omega)\cdot\mathbf{D}^{<}_{mn}(\omega) - \mathbf{D}^{>}_{nm}(\omega)\cdot\mathbf{\Pi}^{<}_{mn}(\omega)). \tag{A13}$$

Each element composing the out-scattering rate $E\mathrm{Tr}(\mathbf{\Sigma}^{>}_{nm}(E)\cdot\mathbf{G}^{<}_{mn}(E))$ in Eq. (A12) has a corresponding element in the in-scattering rate $\hbar\omega\mathrm{Tr}(\mathbf{D}^{>}_{nm}(\omega)\cdot\mathbf{\Pi}^{<}_{mn}(\omega))$ in Eq. (A13) so that they cancel each other:

$$\begin{aligned}&\frac{1}{\hbar}\sum_{nm}\sum_{\sigma_1\sigma_2}\int\frac{dE}{2\pi}E\Bigg(i\sum_{n_1m_1}\sum_{ij}\sum_{\sigma_3\sigma_4}\int\frac{d(\hbar\omega)}{2\pi}\nabla_i H^{\sigma_1\sigma_3}_{nn_1}G^{>\sigma_3\sigma_4}_{n_1m_1}(E-\hbar\omega)\nabla_j H^{\sigma_4\sigma_2}_{m_1m}\big(D^{>ij}_{n_1m}(\omega)\\ &\quad - D^{>ij}_{n_1m_1}(\omega) - D^{>ij}_{nm}(\omega) + D^{>ij}_{nm_1}(\omega)\big)\Bigg)G^{<\sigma_2\sigma_1}_{mn}(E)\\ &= \frac{1}{\hbar}\sum_{n_2m_2}\sum_{i_1j_1}\int\frac{d(\hbar\omega')}{2\pi}\hbar\omega'\big(D^{>i_1j_1}_{n_2m_2}(\omega')\Pi^{<j_1i_1}_{m_2n_2}(\omega')\big).\end{aligned} \tag{A14}$$

The same relationship can be established between the in-scattering rate in Eq. (A12) and the out-scattering rate in Eq. (A13), leading to the following expression for the phonon-electron scattering self-energies:

$$\begin{aligned}\Pi^{\gtrless ij}_{nm}(\omega) = 2_{\mathrm{spin}}\cdot i\sum_{n_1m_1}\sum_{\sigma_1\sigma_2\sigma_3\sigma_4}\int\frac{dE}{2\pi}\big(&\nabla_i H^{\sigma_3\sigma_1}_{n_1n}G^{\gtrless\sigma_1\sigma_4}_{nm_1}(\hbar\omega+E)\nabla_j H^{\sigma_4\sigma_2}_{m_1m}G^{\lessgtr\sigma_2\sigma_3}_{mn_1}(E)\\ &- \nabla_i H^{\sigma_3\sigma_1}_{n_1n}G^{\gtrless\sigma_1\sigma_2}_{nm}(\hbar\omega+E)\nabla_j H^{\sigma_2\sigma_4}_{mm_1}G^{\lessgtr\sigma_4\sigma_3}_{m_1n_1}(E) - \nabla_i H^{\sigma_1\sigma_3}_{nn_1}G^{\gtrless\sigma_3\sigma_4}_{n_1m_1}(\hbar\omega+E)\nabla_j H^{\sigma_4\sigma_2}_{m_1m}G^{\lessgtr\sigma_2\sigma_1}_{mn}(E)\\ &+ \nabla_i H^{\sigma_1\sigma_3}_{nn_1}G^{\gtrless\sigma_3\sigma_2}_{n_1m}(\hbar\omega+E)\nabla_j H^{\sigma_2\sigma_4}_{mm_1}G^{\lessgtr\sigma_4\sigma_1}_{m_1n}(E)\big).\end{aligned} \tag{A15}$$

APPENDIX B: NUMERICAL IMPLEMENTATION

The computational burden is too large to simulate the device described in Sec. III on a single processor or on small clusters. The results presented in this work are obtained by using $N_{\mathrm{CPU}} = 4500$ cores. The N_{CPU} are distributed according to the number of electron energy ($N_E^{\mathrm{el}} \sim 1000$) and phonon frequency ($N_\omega^{\mathrm{ph}} \sim 120$) points that are retained in Eqs. (1)–(6), respectively. This means that around 90% of the cores solve the electron system and 10% the phonon one. First the ballistic solution is calculated by setting the scattering self-energies to zero. Then, at the beginning of each self-consistent Born iteration, the CPUs dealing with phonon Green's functions send their $\mathbf{D}^{<>}(\omega)$ to the CPUs dedicated to the electrons. The latter ones solve Eqs. (14)–(16) to evaluate $\mathbf{\Sigma}^{<>}(E)$ and $\mathbf{\Pi}^{<>}(\omega)$ and then send the phonon-electron self-energies $\mathbf{\Pi}^{<>}(\omega)$ back to the phonon CPUs.

The scaling performance of the fully coupled approach (self-heating) described in this work and of the standard scattering approach of Ref. [22] is reported in Fig. 10 for a reduced nanowire system with $d = 3$ nm, 7141 atoms, $N_E^{\mathrm{el}} = 895$, and $N_\omega^{\mathrm{ph}} = 31$. It is shown that the simulation time for one Born iteration in the fully coupled case is about two times longer than in the standard scattering case where no $\mathbf{\Pi}^{<>}(\omega)$ are calculated. Note that in the self-heating simulations more cores need to be allocated (~ 120) than in the standard scattering case to be able to simultaneously solve the electron and phonon system. As a consequence, the scaling behavior of the fully coupled simulation approach is not as good as in the standard case due to the increase of interprocessor communication.

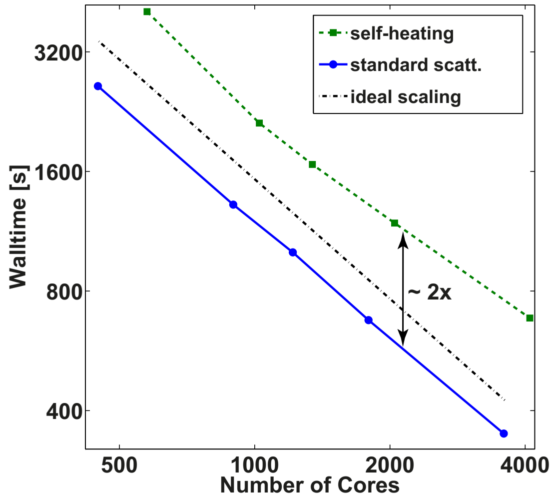

FIG. 10. (Color online) Parallel execution time on a CRAY XE6 for the calculation of one self-consistent Born iteration in the standard scattering (blue solid line with circles), as in Ref. [22], and the self-heating case (dashed green line with squares), i.e., the solution of Eqs. (1)–(6) and (14)–(16) for all electron energies (N_E^{el}) and phonon (N_ω^{ph}) frequencies. The test structure is a nanowire with $d = 3$ nm, a total length of 20 nm, $N_E^{\mathrm{el}} = 895$, $N_\omega^{\mathrm{ph}} = 31$, and a total number of atoms $N_A = 7141$.

[1] G. E. Moore, Electronics **38**, 114 (1965).
[2] W. Haensch *et al.*, IBM J. Res. Dev. **50**, 339 (2006).
[3] P. Zhou, J. Hom, G. Upadhya, K. Goodson, and M. Munch, in *Proceedings of the Semiconductor Thermal Measurement and Management Symposium* (IEEE, Piscataway, 2004), pp. 26–29.
[4] http://www.intel.com/content/www/us/en/silicon-innovations/intel-22nm-technology.html
[5] J. Appenzeller, J. Koch, M. I. Bjork, H. Riel, H. Schmid, and W. Riess, IEEE Trans. Elec. Dev. **55**, 2827 (2008).
[6] A. Hellemans, IEEE Spectrum **50**, 14 (2013).
[7] H. Riel, K. E. Moselund, C. Bessire, M. T. Björk, A. Schenk, H. Ghoneim, and H. Schmid, in *IEDM Technical Digest* (IEEE International, Piscataway, 2012), pp. 391–394.
[8] Y. Cui, Z. Zhong, D. Wang, J. Wang, and C. M. Lieber, Nano Lett. **3**, 149 (2003).
[9] N. Singh *et al.*, IEEE Elec. Dev. Lett. **27**, 383 (2006).
[10] S. Bangsaruntip *et al.*, in *IEDM Technical Digest* (IEEE International, Piscataway, 2009), p. 12.3.
[11] E. Pop *et al.*, Proc. IEEE **94**, 1587 (2006).
[12] D. Li, Y. Wu, P. Kim, L. Shi, P. Yang, and A. Majumdar, Appl. Phys. Lett. **83**, 2934 (2003).
[13] J. P. Feser *et al.*, J. Appl. Phys. **112**, 114306 (2012).
[14] S. Karg *et al.*, J. Electron. Mater. **42**, 2409 (2013).
[15] F. Menges, H. Riel, A. Stemmer, and B. Gotsmann, Nano Lett. **12**, 596 (2012).
[16] K. Souissi, F. Odeh, H. H. K. Tang, and A. Gnudi, COMPEL **13**, 439 (1994).
[17] D. Vasileska, K. Raleva, A. Hossain, and S. M. Goodnick, J. Comput. Electron. **11**, 238 (2012).
[18] Y. Asai, Phys. Rev. B **78**, 045434 (2008).
[19] A. Pecchia, G. Romano, and A. Di Carlo, Phys. Rev. B **75**, 035401 (2007).
[20] R. Rhyner and M. Luisier, in *IEDM Technical Digest* (IEEE International, Piscataway, 2013), p. 32.1.
[21] G. Romano and A. Di Carlo, IEEE Trans. Nanotechnol. **10**, 1285 (2011).
[22] M. Luisier and G. Klimeck, Phys. Rev. B **80**, 155430 (2009).
[23] M. Luisier, A. Schenk, W. Fichtner, and G. Klimeck, Phys. Rev. B **74**, 205323 (2006).
[24] T. B. Boykin, G. Klimeck, and F. Oyafuso, Phys. Rev. B **69**, 115201 (2004).
[25] J. C. Slater and G. F. Koster, Phys. Rev. **94**, 1498 (1954).
[26] S. Lee, F. Oyafuso, P. von Allmen, and G. Klimeck, Phys. Rev. B **69**, 045316 (2004).
[27] M. Luisier, Phys. Rev. B **86**, 245407 (2012).
[28] Z. Sui and I. P. Herman, Phys. Rev. B **48**, 17938 (1993).
[29] A. Paul, M. Luisier, and G. Klimeck, J. Comput. Electron. **9**, 160 (2010).
[30] R. Rhyner and M. Luisier, J. Appl. Phys. **114**, 223708 (2013).
[31] W. Zhang, C. Delerue, Y. M. Niquet, G. Allan, and E. Wang, Phys. Rev. B **82**, 115319 (2010).
[32] A. Fetter and J. Walecka, *Quantum Theory of Many-Particle Systems* (McGraw-Hill, New York, 1971).
[33] H. Haug and A. P. Jauho, *Quantum Kinetics in Transport and Optics of Semiconductors* (Springer, Berlin, 1989).
[34] S. Datta, *Electronic Transport in Mesoscopic Systems* (Cambridge University Press, Cambridge, 1995).
[35] C. Rivas, R. Lake, W. R. Frensley, G. Klimeck, P. E. Thompson, K. D. Hobart, S. L. Rommel, and P. R. Berger, J. Appl. Phys. **94**, 5005 (2003).
[36] U. Aeberhard and R. H. Morf, Phys. Rev. B **77**, 125343 (2008).
[37] A. Svizhenko and M. P. Anantram, Phys. Rev. B **72**, 085430 (2005).
[38] S. Jin, Y. J. Park, and H. S. Min, J. Appl. Phys. **99**, 123719 (2006).
[39] R. Lake, G. Klimeck, R. C. Bowen, and D. Jovanic, J. Appl. Phys. **81**, 7845 (1997).
[40] A. Svizhenko, M. P. Anantram, T. R. Govindan, B. Biegel, and R. Venugopal, J. Appl. Phys. **91**, 2343 (2002).
[41] M. Frey, A. Esposito, and A. Schenk, *Proceedings of the 38th European Solid-State Device Research Conference (ESSDERC)* (IEEE, Piscataway, NJ, 2008), p. 258.
[42] A. Svizhenko and M. P. Anantram, IEEE Trans. Electron Devices **50**, 1459 (2003).
[43] M. S. Lundstrom, IEEE Electron Device Lett. **22**, 293 (2001).
[44] M. Galperin, A. Nitzan, and M. A. Ratner, Phys. Rev. B **75**, 155312 (2007).
[45] G. Romano, A. Gagliardi, A. Pecchia, and A. Di Carlo, Phys. Rev. B **81**, 115438 (2010).
[46] M. Büttiker, Phys. Rev. B **33**, 3020 (1986).
[47] S. Hershfield, Phys. Rev. Lett. **70**, 2134 (1993).